Available online at www.sciencedirect.com

ScienceDirect

Geochimica et Cosmochimica Acta 191 (2016) 102–117

Geochimica et Cosmochimica Acta

www.elsevier.com/locate/gca

Stable silicon isotope signatures of marine pore waters – Biogenic opal dissolution versus authigenic clay mineral formation

Claudia Ehlert [a,*], Kristin Doering [a,b], Klaus Wallmann [a], Florian Scholz [a], Stefan Sommer [a], Patricia Grasse [a,1], Sonja Geilert [a], Martin Frank [a]

[a] GEOMAR Helmholtz Centre for Ocean Research Kiel, Germany
[b] Institute of Geoscience, Department of Geology, Kiel University, Germany

Received 16 November 2015; accepted in revised form 14 July 2016; Available online 22 July 2016

Abstract

Dissolved silicon isotope compositions have been analysed for the first time in pore waters ($\delta^{30}Si_{PW}$) of three short sediment cores from the Peruvian margin upwelling region with distinctly different biogenic opal content in order to investigate silicon isotope fractionation behaviour during early diagenetic turnover of biogenic opal in marine sediments. The $\delta^{30}Si_{PW}$ varies between +1.1‰ and +1.9‰ with the highest values occurring in the uppermost part close to the sediment–water interface. These values are of the same order or higher than the $\delta^{30}Si$ of the biogenic opal extracted from the same sediments (+0.3‰ to +1.2‰) and of the overlying bottom waters (+1.1‰ to +1.5‰). Together with dissolved silicic acid concentrations well below biogenic opal saturation, our collective observations are consistent with the formation of authigenic alumino-silicates from the dissolving biogenic opal. Using a numerical transport-reaction model we find that approximately 24% of the dissolving biogenic opal is re-precipitated in the sediments in the form of these authigenic phases at a relatively low precipitation rate of 56 μmol Si cm^{-2} yr^{-1}. The fractionation factor between the precipitates and the pore waters is estimated at −2.0‰. Dissolved and solid cation concentrations further indicate that off Peru, where biogenic opal concentrations in the sediments are high, the availability of reactive terrigenous material is the limiting factor for the formation of authigenic alumino-silicate phases.

Keywords: Silicon isotopes; Pore water; Silicic acid; Biogenic opal; Authigenic alumino-silicates

1. INTRODUCTION

The Peruvian upwelling region is characterised by high diatom primary productivity (Estrada and Blasco, 1985; Bruland et al., 2005). As the diatom valves (biogenic opal) sink down about 92% dissolve in the water column and/or below the sediment – water interface (Tréguer and De La Rocha, 2013 and references therein). Therefore, silicic acid concentrations increase with increasing water depth, especially in the water column of shallow shelf regions. As a result of the high diatom primary productivity, the underlying sediments are rich in biogenic opal (Abrantes et al., 2007).

Previous studies have shown that the Peru – Chile Undercurrent gets strongly enriched in silicic acid along its flow path from 15 μM prior to its contact with the northern Peruvian shelf to 40 μM above the shelf at 12°S (Ehlert et al., 2012). These bottom waters of the shelf stations have a lower dissolved silicon isotope composition ($\delta^{30}Si$) than

* Corresponding author at: Max Planck Research Group for Marine Isotope Geochemistry, Institute for Chemistry and Biology of the Marine Environment (ICBM), University of Oldenburg, Germany.
E-mail address: cehlert@mpi-bremen.de (C. Ehlert).
[1] University of California Santa Barbara, USA.

http://dx.doi.org/10.1016/j.gca.2016.07.022
0016-7037/

waters further offshore at the same water depth, which have not been in contact with the shelf sediments (Grasse et al., 2013). The potential reason for this pattern is the higher fluxes and concentrations of isotopically light biogenic opal above the shelf and its dissolution in the water column. Also, benthic dissolution of diatom opal could result in a flux of isotopically light silicon from the sedimentary pore waters into the bottom water.

In general, most of the biogenic opal deposited on the seafloor dissolves rapidly in the silica under-saturated bottom waters. However, a significant fraction is preserved and matures. Moreover, authigenic silicate phases are formed in near-surface sediments by the precipitation of silica, aluminium (Al), iron (Fe) and seawater solutes (Mackin, 1987). In opal-rich sediments, the formation of these authigenic phases is limited by Al and Fe released from reactive terrigenous phases (Loucaides et al., 2010; Van Cappellen and Qiu, 1997a) whereas biogenic opal is the limiting factor in river delta sediments containing abundant Al- and Fe-bearing phases including metal oxides, feldspars, and clays (Michalopoulos and Aller, 1995). Authigenic Fe-, potassium (K)- and magnesium (Mg)-rich alumino-silicates, often described as glauconite or green clay, are major alteration products of biogenic opal in marine sediments (Loucaides et al., 2010; Michalopoulos and Aller, 2004). In terrigenous sediments of the Amazon delta these authigenic phases form at a rate as high as 280 μmol Si cm^{-2} yr^{-1} (Michalopoulos and Aller, 2004). In hemipelagic sediments their formation is focused in the topmost layer of the sediment column (ca. 0–5 cm sediment depth) where dissolved Al and Fe are released from metal oxides and reactive alumino-silicates (Mackin and Aller, 1984; Van Cappellen and Qiu, 1997a).

The main goal of this study is to investigate dissolution of biogenic opal and the potential formation of authigenic alumino-silicate phases during early diagenesis of biogenic opal in marine sediments off Peru. For this purpose, we analysed three short sediment cores from different water depths across the Peruvian shelf at 11°S for their biogenic opal and silicic acid concentrations in the pore waters, the silicic acid flux to the overlying bottom waters, and solid phase and selected dissolved cation concentrations. These parameters were for the first time combined with the stable silicon isotope composition of the sedimentary biogenic opal ($\delta^{30}Si_{bSi}$) and of the silicic acid in the pore waters ($\delta^{30}Si_{PW}$). Based on these data, we use a numerical transport-reaction model to constrain the benthic rates of biogenic opal dissolution, authigenic mineral precipitation, and overall reaction fractionation factors.

2. MATERIALS AND METHODS

The three sediment cores for this study were recovered with a multiple corer (MUC) along a depth transect at 11°S at the Peruvian shelf from 145 m (core 470-MUC29), 319 m (core 449-MUC19) and 1005 m (core 549-MUC53) water depth during cruise M77/1 with the German R/V Meteor in October–November 2008 (Table 1). Details on the age models and sedimentation rates of the three cores can be found in the Supplement.

The cores were transferred to a cool room (4 °C) immediately after recovery and were processed within a few hours. Samples for bottom water analysis were taken from the supernatant water of the sediment cores within 1 h after core retrieval. After removal of overlying water, MUCs were sampled under oxygen-free conditions using an argon-filled glove bag, given that redox-sensitive elements were also analysed from sample aliquots. Sediment sections for pore water extraction were transferred into 50 mL centrifuge tubes pre-flushed with argon gas and subsequently centrifuged at max. 4500 rpm for 20 min. The supernatant pore waters were filtered through 0.2 μm cellulose acetate Nuclepore® filters within the glove bag. Silicic acid concentrations were measured on board colorimetrically using standard photometric techniques (Grasshoff et al., 1999) (Fig. 1, Table 1). Pore water subsamples (0.5 cm^3) were diluted to 5 cm^3 with pure water, 0.2 cm^3 of heptamolybdate solution was added, and the samples were shaken vigorously. After 30 min, 0.2 cm^3 oxalic acid and 0.2 cm^3 ascorbic acid were added to the sample. About 30 min later, the absorbance was measured at 810 nm.

2.1. In situ flux measurements

In situ fluxes of silicic acid from the sediments close to core 449-MUC19 were measured using the Biogeochemical Observatory BIGO-T as described in detail by Sommer et al. (2009) at two sites at 305 m water depth (535-BIGO-T3) and 309 m water depth (566-BIGO-T4) from within the Peruvian oxygen minimum zone during the same cruise (Fig. 2, Table 2). At these sites oxygen levels were <2 μM.

BIGO-T observatories contained one circular flux chamber (internal diameter 28.8 cm, area 651.4 cm^2). A TV–guided launching system allowed smooth emplacement of the observatories at selected sites on the sea floor. Two hours after the observatories were placed on the sea floor the chamber was slowly driven into the sediment (ca. 30 cm h^{-1}). During this initial time period, the water inside the flux chamber was replaced four times with ambient bottom water. After the chamber was fully driven into the sediment, the chamber water was again replaced with ambient bottom water to flush out solutes that might have been released from the sediment during chamber insertion. The water volume enclosed by the benthic chamber in BIGO-T3 and BIGO-T4 was 9.93 and 9.53 L respectively. During the deployments of BIGO-T, the chamber water was replaced with ambient bottom water half way through the incubation period to restore outside conditions and repeat the benthic flux measurement.

To determine silicic acid fluxes, four sequential water samples were removed with glass syringes (volume of each syringe ca. 47 mL). During the deployments of BIGO-T, a series of four water samples were taken before and after the chamber water was replaced. Two fluxes were calculated for silicic acid, one for the first series of water samples taken prior to the replacement of the chamber water denoted as I1, and another one for the second series of water samples (I2). The flux measurements for I1 and I2 were conducted for 10 h. The syringes were connected to the chamber using

Table 1
Data for solid phase (biogenic opal (bSi), $\delta^{30}Si_{bSi}$, porosity, Al, K and porosity-corrected K concentrations) and pore waters (silicic acid (Si), $\delta^{30}Si_{PW}$, dissolved K and Cl concentrations) for the three cores.

Profile depth	Solid phase						Pore water				
(cm)	bSi (wt%)	$\delta^{30}Si_{bSi}$ (‰)	$2\sigma_{sd}$	Porosity	Al (mg/g)	K (porosity corrected) (mg/g)	Si (μM)	$\delta^{30}Si_{PW}$ (‰)	$2\sigma_{sd}$	K (mM)	Cl (mM)
M77/1-470-MUC29											
Bottom water	–	–	–	–	–	–	36.4	–	–	10.2	557
0.5	18.8	+1.03	0.15	0.953	39.30	9.54	325.0	–	–	10.2	559
1	–	–	–	–	–	–	–	+1.21	0.04	–	–
1.5	18.6	–	–	0.944	47.82	10.70	448.0	–	–	10.2	562
2.5	22.2	–	–	0.945	49.12	11.11	632.0	–	–	10.2	559
3.5	16.9	+0.93	0.08	0.940	48.96	10.85	722.0	–	–	10.3	559
4.5	16.3	–	–	0.932	48.35	10.97	795.0	–	–	10.3	556
5	–	–	–	–	–	–	–	+1.41	0.21	–	–
5.5	17.2	–	–	0.938	46.54	10.53	772.0	–	–	10.2	557
7	19.5	–	–	0.955	40.91	8.69	806.0	–	–	10.3	558
9	19.8	+0.96	0.09	0.935	53.30	11.24	842.0	–	–	10.3	558
11	18.8	–	–	0.928	50.70	11.19	834.0	–	–	10.0	564
13	15.9	–	–	0.925	50.68	11.30	838.0	+1.23	0.11	10.2	537
16	19.3	+0.96	0.07	0.920	49.51	11.17	858.5	–	–	10.2	565
20	18.9	+1.05	0.1	0.915	48.71	10.80	898.0	–	–	10.2	543
21	–	–	–	–	–	–	–	+1.33	0.20	–	–
24	26.9	+1.15	0.13	0.920	45.17	10.12	892.5	–	–	10.3	545
25	–	–	–	–	–	–	–	+1.09	0.23	–	–
28	14.0	+1.00	0.14	0.838	36.80	9.36	883.0	–	–	10.1	545
32	–	+0.55	0.17	0.818	–	–	–	–	–	–	–
32.5	10.1	–	–	–	62.56	14.15	863.0	–	–	9.7	560
33	–	–	–	–	–	–	–	+1.13	0.02	–	–
36	–	+1.10	0.15	0.846	–	–	–	–	–	–	–
37.5	14.4	–	–	–	58.12	13.13	888.0	–	–	10.0	562
40	–	+0.79	0.11	0.822	–	–	–	–	–	–	–
42.5	12.3	–	–	–	61.02	14.36	853.5	–	–	10.1	563
44	–	+0.91	0.18	0.841	–	–	–	–	–	–	–
47.5	15.0	–	–	–	60.10	13.52	860.5	–	–	10.2	563
48	–	+0.75	0.05	0.839	–	–	–	–	–	–	–
M77/1-449-MUC19											
Bottom water	–	–	–	–	–	–	41.4	+1.40	0.18	9.8	554
0.5	12.4	–	–	0.958	22.27	5.26	357.2	–	–	9.9	552
1.5	5.7	–	–	0.939	27.90	6.92	363.2	–	–	9.8	546
2.5	4.4	–	–	0.944	28.67	7.17	360.2	–	–	10.0	551
3.5	4.1	+0.44	0.21	0.942	30.36	7.69	359.2	–	–	9.9	551
4	–	–	–	–	–	–	–	+1.73	0.08	–	–
4.5	5.0	–	–	0.936	37.93	9.18	351.2	–	–	10.0	537
5.5	5.4	–	–	0.932	41.00	9.77	346.8	–	–	10.0	550
7	4.4	–	–	0.927	41.25	10.08	370.2	–	–	9.8	547
8	–	–	–	–	–	–	–	+1.93	0.15	–	–
9	4.2	–	–	0.927	39.03	9.38	397.2	–	–	10.0	541
11	–	+0.58	0.19	0.925	37.14	8.79	426.8	–	–	9.8	552
12	–	–	–	–	–	–	–	+1.60	0.14	–	–
13	3.8	–	–	0.920	37.25	8.80	478.0	–	–	10.0	552
16	4.6	+0.30	0.26	0.910	42.23	10.56	511.6	+1.57	0.15	9.8	548
20	5.2	–	–	0.902	48.86	11.91	602.6	–	–	9.9	551
24	7.3	+0.47	0.15	0.903	47.56	11.70	657.6	+1.79	0.09	10.0	554
28	11.6	–	–	0.899	45.11	11.09	697.4	–	–	9.9	544
32	9.3	–	–	0.893	–	–	–	+1.60	0.16	–	–
32.5	–	–	–	–	46.09	11.60	727.8	–	–	9.7	551
36	7.7	+1.16	0.17	0.892	–	–	–	+1.56	0.15	–	–
37.5	–	–	–	–	46.07	11.72	743.0	–	–	9.8	544
40	7.7	–	–	0.885	–	–	–	–	–	–	–
42.5	–	–	–	–	47.11	12.14	745.6	–	–	10.0	549
44	7.5	+1.20	0.17	0.888	–	–	–	+1.36	0.04	–	–
47.5	–	–	–	–	39.88	10.27	758.2	–	–	9.8	542
48	7.3	–	–	0.876	–	–	–	–	–	–	–

M77/1-459-MUC53											
Bottom water	–	–	–	–	–	–	61.2	–	–	10.0	553
0.5	2.0	–	–	0.818	42.13	12.95	195.2	–	–	10.1	559
1.5	1.9	–	–	0.794	42.20	12.56	207.0	–	–	10.3	561
2	–	–	–	–	–	–	–	+1.68	0.15	–	–
2.5	1.6	–	–	0.772	43.50	13.46	218.2	–	–	10.4	557
3.5	2.0	–	–	0.760	42.90	13.48	243.4	–	–	10.5	559
4	–	–	–	–	–	–	–	+1.70	0.07	–	–
4.5	–	–	–	–	44.03	14.55	261.0	–	–	10.4	562
5	1.6	–	–	0.740	–	–	–	–	–	–	–
5.5	–	–	–	–	43.67	14.47	259.6	–	–	10.4	558
6	–	–	–	–	–	–	–	+1.37	0.06	–	–
7	1.6	–	–	0.710	45.38	15.90	293.8	–	–	10.6	566
9	1.4	–	–	0.678	44.52	15.51	322.2	–	–	10.6	558
10	–	–	–	–	–	–	–	+1.48	0.03	–	–
11	1.3	–	–	0.720	–	–	–	–	–	–	–
12	–	–	–	–	44.74	15.21	347.0	–	–	10.4	557
14	1.4	–	–	0.715	–	–	–	–	–	–	–
16	–	–	–	–	45.20	15.18	376.4	+1.40	0.11	10.4	557
18	–	–	–	–	–	–	–	+1.28	0.06	–	–
20	–	–	–	–	–	–	–	+1.34	0.04	–	–
20.5	–	–	–	–	41.69	13.55	342.2	–	–	10.5	555
25.5	–	–	–	–	36.06	12.41	328.2	–	–	10.8	559

1 m long Vygon tubes with a dead volume of 6.9 mL. Prior to deployment, these tubes were filled with distilled water, and great care was taken to avoid enclosure of air bubbles. Immediately after retrieval of the observatories, the water samples were transferred to the onboard cool room (4 °C) for further sample processing and sub-sampling. Chloride concentrations were determined to correct for dilution with fresh water and the silicic acid fluxes were calculated from the linear increase of the corrected silicic acid concentrations with time (Fig. 2).

2.2. Sample preparation and measurements

For major element analyses, 100 mg of freeze dried and ground sediment sample was digested in HF (40%, supra pure), HNO_3 (65%, supra pure) and $HClO_4$ (60%, p.a.). The accuracy of the digestion procedure was monitored by including method blanks and the reference standards SDO-1 (Devonian Ohio Shale, USGS; Govindaraju, 1994) and MESS-3 (Marine Sediment Reference Material, Canadian Research Council) in the digestion procedure. Selected cation concentrations in pore water samples and digestion solutions were determined by inductively coupled plasma optical emission spectrometry (ICP-OES, VARIAN 720-ES). The K and Al concentrations measured for SDO-1 and MESS-3 were well within the certified ranges and the reproducibility was <2% relative standard deviation.

For dissolved $\delta^{30}Si_{PW}$ measurements, the samples were treated following the method of Georg et al. (2006). No preconcentration of Si was necessary because the concentration of silicic acid relative to its salt content is much higher in pore waters than in seawater. Samples were diluted to equal Si concentrations using MilliQ-water (18.2 MΩ), were then loaded directly onto pre-cleaned BioRad columns filled with 1 mL cation exchange resin AG50 W-X8 (Georg et al., 2006; de Souza et al., 2012), and were eluted typically using 2 mL of MilliQ-water. The determination of the Si isotope composition can be susceptible to the complex matrix composition in a sample, i.e., anions and dissolved organic matter (e.g., Van den Boorn et al., 2009; Hughes et al., 2011). Therefore, several tests were executed in order to check for those matrix effects. Aliquots of a pore water sample were treated with Ba to remove SO_4 by precipitation of barite. Organic matter was removed by the addition of hydrogen peroxide and left on the hotplate until the reaction ceased. Every test was executed for three aliquots of the same pore water sample. Subsequently all test solutions were measured on the NuPlasma MC-ICPMS (Nu Instruments) at GEOMAR together with three aliquots of the untreated sample. The average $\delta^{30}Si$ in all three tests was +1.3‰ and was identical within analytical precision (see Supplementary Table S2). The standard deviation of the individual measurements and aliquots was higher for the samples treated with Ba ($2\sigma_{sd} = 0.6$‰) than for the untreated sample ($2\sigma_{sd} = 0.2$‰) and the sample treated with hydrogen peroxide ($2\sigma_{sd} = 0.2$‰). Consequently no matrix effects affected the Si isotope measurements on the NuPlasma MC-ICPMS and no sample pretreatment or standard doping was necessary for the pore water measurements.

For the $\delta^{30}Si_{bSi}$ the size fraction 11–32 μm was chosen because it contained a high abundance of different diatoms species while at the same time it was generally not compromised significantly by other biogenic opal material such as radiolarian fragments or sponge spicules. Larger diatoms species like *Coscinodiscus* were usually also present as fragments (Ehlert et al., 2012; Doering et al., 2016). The diatoms were separated from the sediment using established chemical and physical cleaning techniques (sieving and heavy liquid separation) as described by Morley et al. (2004). All samples were scanned via light microscopy to verify their purity with respect to the detrital (clay) fraction and other opal phases (radiolarians, sponge spicules) prior to dissolution. Only pure (>95%) diatom samples were

further treated. Sample aliquots were transferred into Teflon vials and dissolved in 1 mL 0.1 M NaOH at 130 °C for 12 h. Residual material was separated via centrifugation and remaining organic matter was removed by adding 200 µL concentrated H_2O_2 (Suprapur). Sample solutions were diluted with 4 mL MilliQ water, neutralised with 0.1 mL 1 M HCl, and purified using ion chromatography (Reynolds et al., 2008).

Si isotope ratios were measured on the NuPlasma HR MC-ICPMS (Nu Instruments) at GEOMAR in medium resolution mode. Samples were introduced into the plasma via a Cetac Aridus II desolvator equipped with a PFA nebulizer at a 60–80 µL min^{-1} uptake rate and were usually measured at Si concentrations of 14–21 µM depending on the sensitivity of the instrument during each session. Measurements were carried out with a standard-sample bracketing method (Albarède et al., 2004). Silicon isotope compositions are reported in the $\delta^{30}Si$ notation as deviations of the measured $^{30}Si/^{28}Si$ from the international Si standard NBS28 in parts per thousand (‰). Repeated

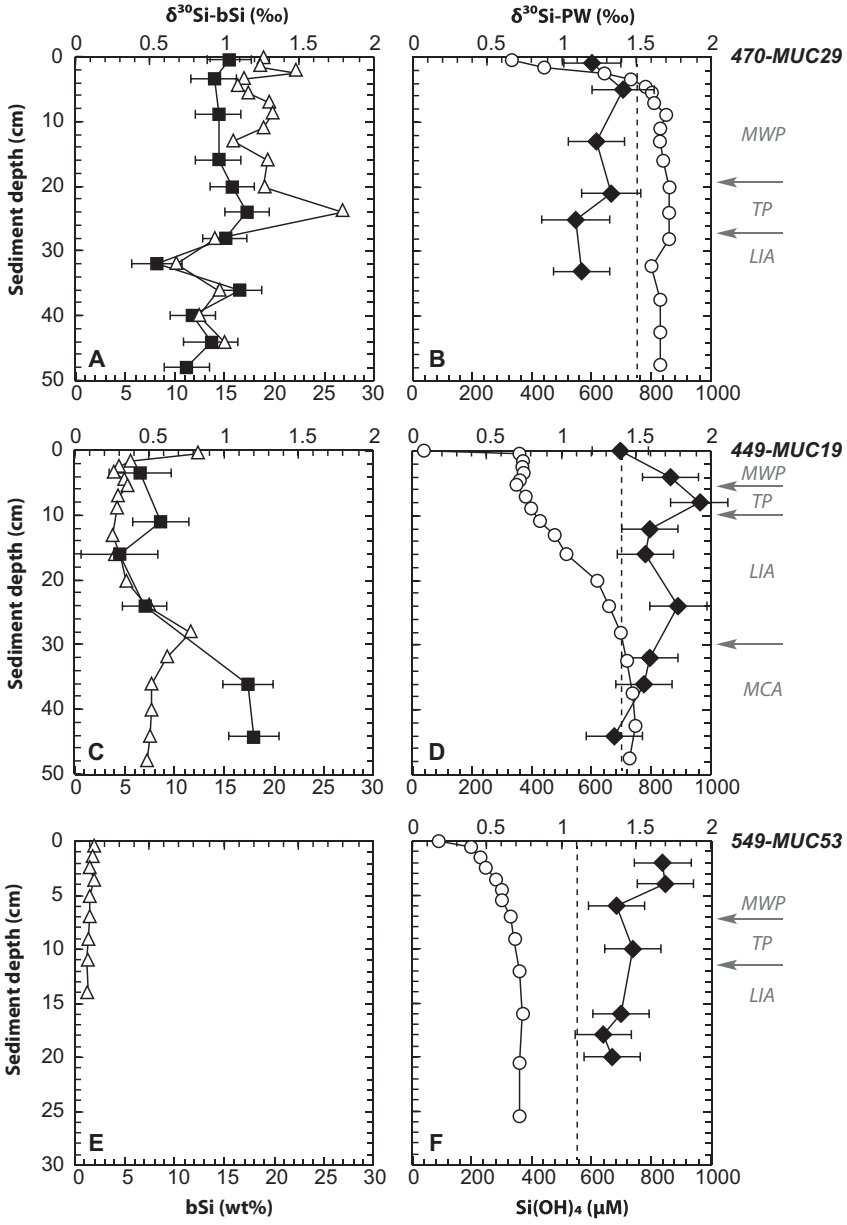

Fig. 1. Profiles for (A, C, E) biogenic opal (wt%, white triangles) and $\delta^{30}Si_{bSi}$ (‰, black squares) and (B, D, F) silicic acid (µM, white circles) and $\delta^{30}Si_{PW}$ (‰, black diamonds) for the three sites (top: 470-MUC29, middle: 449-MUC19, bottom: 549-MUC53). The dashed lines indicate the overlying bottom water/seawater $\delta^{30}Si$ (470-MUC29: +1.5‰, 449-MUC19: +1.4‰, 549-MUC53: +1.1‰; Ehlert et al., 2012; Grasse et al., 2013, and this study). Arrows indicate the approximate transition for major climatic periods: MWP – Modern Warm Period, TP – Transition Period, LIA – Little Ice Age, MCA – Medieval Climate Anomaly (see Supplement for details).

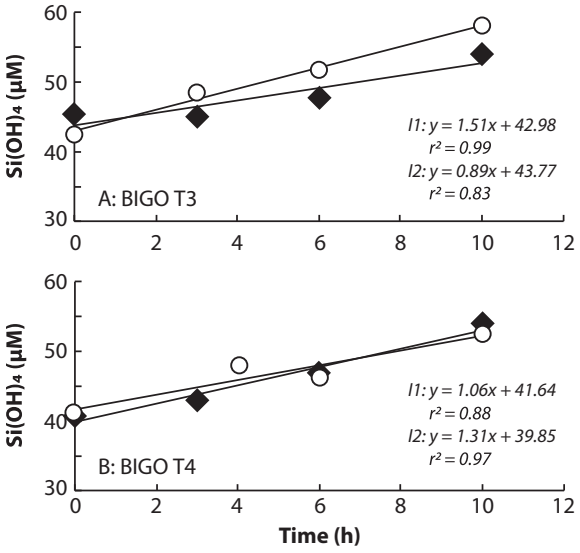

Fig. 2. Concentrations of silicic acid (µM) during the chamber flux measurements inside the OMZ at 305 m water depth (BIGO-T3) and 309 m water depth (BIGO-T4). Repeat flux experiments were conducted within the same chamber, where the enclosed water body was replaced after about 10 h. I1 (white circles) and I2 (black diamonds) denote the incubation period before and after replacement of the chamber water, respectively.

measurements of the reference materials IRMM018, Big Batch (an isotopically highly fractionated SiO_2 standard produced by precipitation of dissolved sodium metasilicate; Brzezinski et al., 2006) and Diatomite gave average $\delta^{30}Si$ values of -1.44 ± 0.11‰ ($2\sigma_{sd}$, $n = 18$), -10.63 ± 0.18‰ and $+1.20 \pm 0.08$‰, respectively, which are in good agreement with values obtained by other laboratories (Reynolds et al., 2007). Samples were measured three to five times during a daily session, and were measured two to three times on different days resulting in reproducibilities between ±0.02‰ and ±0.26‰ ($2\sigma_{sd}$) (Table 1). Replicate measurements of an in–house pore water matrix standard gave a reproducibility of ±0.19‰ ($2\sigma_{sd}$, $n = 8$) and a matrix opal standard was reproduced at ±0.15‰ ($2\sigma_{sd}$, $n = 9$). Error bars provided in the figures correspond to the external reproducibilities of the matrix standards unless the uncertainties of the repeated sample measurements were higher.

2.3. Numerical model set-up

The turnover of biogenic opal and silicic acid in core 449-MUC19 was simulated applying the following mass balance equations:

$$d_s \cdot (1-\Phi) \cdot \frac{\partial \mathrm{bSi}}{\partial t} = \frac{\partial}{\partial x}\left(d_s \cdot (1-\Phi)\left(D_B \cdot \frac{\partial \mathrm{bSi}}{\partial x} - w \cdot \mathrm{bSi}\right)\right) - d_s \cdot (1-\Phi) \cdot R_D$$

$$\Phi \cdot \frac{\partial \mathrm{Si}}{\partial t} = \frac{\partial}{\partial x} \cdot \left(\Phi(D_S \cdot \frac{\partial Si}{\partial x} - v \cdot Si)\right) + \frac{d_s \cdot (1-\Phi)}{M_{SiO_2}} \cdot R_D - \Phi \cdot R_P \quad (2)$$

with d_s: density of dry solids ($d_s = 2.0$ g cm^{-3} for sediments from the Peruvian OMZ; Böning et al., 2004), Φ: porosity; bSi: solid phase concentration of biogenic opal (g SiO_2 g^{-1}), t: time (yr), x: sediment depth (cm), D_B: bioturbation coefficient (cm^2 yr^{-1}), w: burial velocity of solids (cm yr^{-1}), R_D: dissolution rate of biogenic opal (g SiO_2 g^{-1} yr^{-1}), Si: concentration of silicic acid (µmol cm^{-3}), D_S: molecular diffusion coefficient of silicic acid in sediment pore water (cm^2 yr^{-1}), v: burial velocity of pore water (cm yr^{-1}), M_{SiO2}: molecular weight of SiO_2, and R_P: precipitation rate (µmol Si cm^{-3} yr^{-1}).

The partial differential equations above assume steady state compaction, i.e. porosity is allowed to change with sediment depth but not over time. This simplification is justified by the porosity data (Fig. 3A) showing a regular exponential decrease with sediment depth indicative of steady-state compaction (Berner, 1980). The following equation was employed for porosity (Berner, 1980):

$$\Phi = \Phi_f + (\Phi_i - \Phi_f) \cdot e^{-p \cdot x} \quad (3)$$

where the initial porosity at the sediment water interface ($\Phi_i = 0.95$), the porosity after compaction ($\Phi_f = 0.86$), and the attenuation coefficient ($p = 0.07$ cm^{-1}) were determined by fitting the model to the data. The effect of tortuosity on diffusion was considered applying the following empirical equation (Boudreau, 1996):

$$D_s = \frac{D_M}{1 - 2 \cdot \ln \Phi} \quad (4)$$

where the molecular diffusion coefficient for ambient temperature (11.4 °C) and salinity (35) amounts to $D_M = 218$ cm^2 yr^{-1} (Wollast and Garrels, 1971). The bioturbation coefficient (1 cm^2 yr^{-1} at the surface, halving depth 1 cm) and burial velocity after compaction ($w_f = 0.05$ cm yr^{-1})

Table 2
Stations where in situ benthic fluxes of silicic acid were determined (µmol cm^{-2} d^{-1}) along a latitudinal transect at 11°S. Positive fluxes indicate release from the seabed. During the flux measurements of BIGO T, the chamber water was replaced once with ambient seawater halfway through the incubation period. For these deployments, I1 refers to the time interval after driving the chamber into the sediment, I2 refers to the time interval after the chamber water was replaced.

Lander	Chamber/interval	Date (2008)	Position (long. W)	Depth (m)	$T_{inc.}$ (h)	Diss. Si flux (µmol cm^{-2} d^{-1})
BIGO-T4	I1	14.11	78°09.13′	309	20.7	0.37
M77-1–566	I2					0.46
BIGO-T3	I1	12.11	78°15.38′	305	20.7	0.55
M77-1–535	I2					0.33

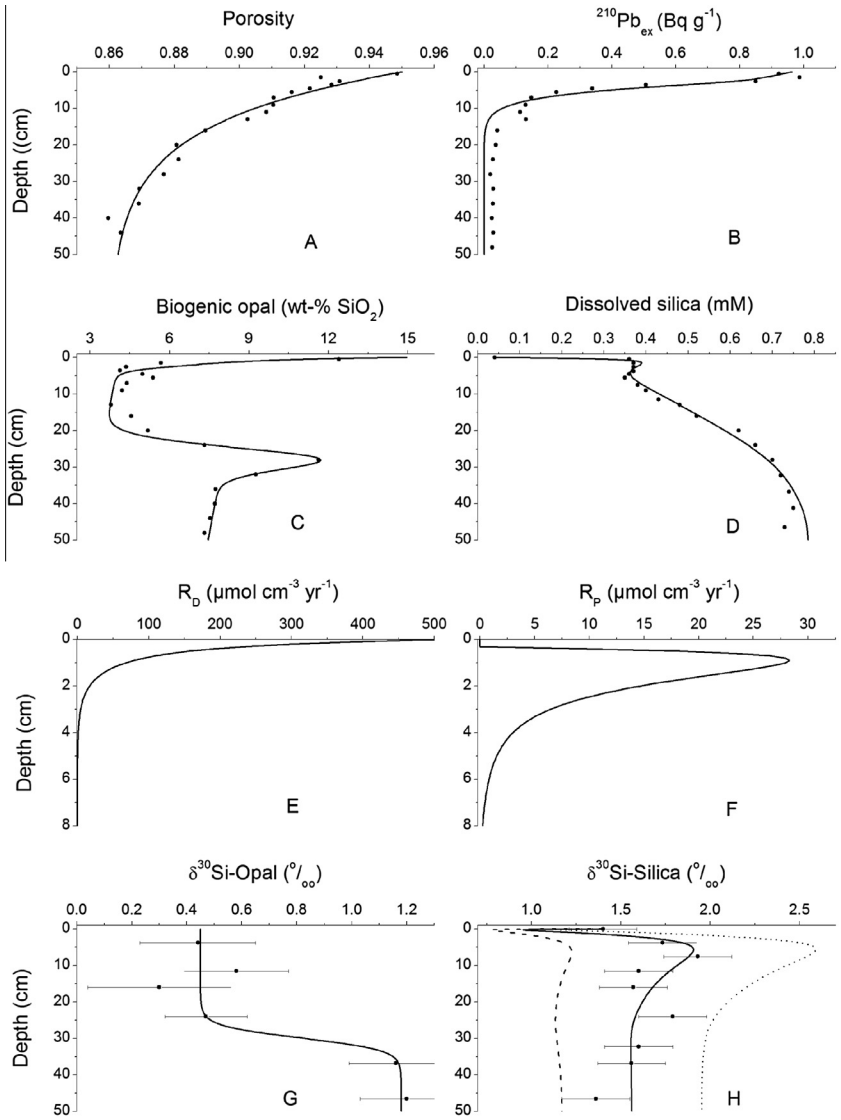

Fig. 3. Model results (lines) versus data (dots) obtained at station 449-MUC19. (A) porosity, (B) excess ^{210}Pb, (C) biogenic opal, (D) silicic acid, (E) rate of biogenic opal dissolution, (F) rate of authigenic mineral precipitation, (G) δ^{30}Si of biogenic opal, H) pore water dissolved δ^{30}Si. The isotopic fraction factor for authigenic mineral precipitation Δ_P was varied from −1‰ (dashed line) to −3‰ (dotted line). The best fit was obtained with −2‰ (solid line).

were derived from ^{210}Pb measurements applying a steady state model (Meysman et al., 2005; Dale et al., 2015). Down-core changes in burial velocity were calculated assuming steady-state compaction (Berner, 1980). However, it should be noted that the burial velocity below 15 cm sediment depth is not constrained by our ^{210}Pb data (Fig. 3B). Since the reactions considered in the model occur mostly within the top 10 cm of the sediment column (Fig. 3E and F), the poorly constrained sedimentation rate below 15 cm depth has no significant effect on the model results.

The kinetic rate law of biogenic opal dissolution (Hurd, 1972) was formulated as:

$$R_D = k_D \cdot \mathrm{bSi} \cdot \left(1 - \frac{\mathrm{Si}}{S_{\mathrm{bSi}}}\right) \quad (5)$$

with R_D: dissolution rate (g SiO_2 g^{-1} yr^{-1}), k_D: kinetic constant (yr^{-1}), bSi: solid phase concentration of biogenic opal (g SiO_2 g^{-1}), Si: silicic acid (mM), and S_{bSi}: solubility of biogenic opal (mM). The kinetic rate law states that the dissolution rate is proportional to the saturation state. However, this first order relationship is not valid in solutions strongly undersaturated with respect to biogenic opal (Si < 0.2 mM) where rates are higher than predicted by the linear rate law (Van Cappellen and Qiu, 1997b). Hence, the kinetic constant k_D was allowed to decrease exponentially with sediment depth to consider this effect and the down-core decrease in reactivity induced by opal maturation (Rickert, 2000; Van Cappellen and Qiu, 1997b). The solubility of biogenic opal at ambient pressure and temperature conditions (11.4 °C, 31.9 bar; Bohlen et al., 2011) was

estimated as $S_{bSi} \approx 1$ mM (Loucaides et al., 2012; Van Cappellen and Qiu, 1997a).

The precipitation of authigenic alumino-silicates was simulated as:

$$R_P = k_P \cdot \left(\frac{Si}{S_A} - 1\right) \quad (6)$$

for $Si > S_A$ and

$$R_P = 0 \quad (7)$$

for $Si \leqslant S_A$

where R_P is the precipitation rate (μmol Si cm^{-3} yr^{-1}), k_P is the kinetic constant (μmol Si cm^{-3} yr^{-1}), and S_A the solubility of the authigenic phase. The rate was thus assumed to be proportional to the degree of oversaturation and set to zero in undersaturated and saturated solutions. However, the saturation is also controlled by the concentration of dissolved Al in pore fluids, which was not measured for the studied cores. Aluminium concentrations are typically high in the top layer of hemipelagic sediments layer where Al is released from reactive Al-bearing phases such as gibbsite, feldspars and volcanic ashes (e.g., Rabouille et al., 1997; Van Beusekom et al., 1997). It is thus reasonable to assume that most of the authigenic alumino-silicate precipitates in the near-surface sediments where dissolved Al is available. Hence, the kinetic constant for precipitation was assumed to decrease exponentially with sediment depth to focus the precipitation process in the near-surface layer. The best fit to the data was attained with k_P (in μmol cm^{-3} yr^{-1}) = 110 exp (−0.7x) + 0.012. The rate law for precipitation applied in the model is purely empirical. It has no theoretical basis and should only be employed in cases where the stoichiometry of the authigenic alumino-silicate phase(s) and the dissolved Al concentrations are unknown.

The isotope model was based on the following mass balance equations for ^{30}Si in biogenic opal ($b^{30}Si$) and silicic acid (^{30}Si):

$$d_S \cdot (1-\Phi) \cdot \frac{\partial b^{30}Si}{\partial t} = \frac{\partial}{\partial x}\left(d_s \cdot (1-\Phi) \cdot \left(D_B \cdot \frac{\partial b^{30}Si}{\partial x} - w \cdot b^{30}Si\right)\right) - d_s \cdot (1-\Phi) \cdot \frac{b^{30}Si}{bSi} \cdot R_D \quad (8)$$

$$\Phi \cdot \frac{\partial {}^{30}Si}{\partial t} = \frac{\partial}{\partial x}\left(\Phi \cdot \left(D_s \cdot \frac{\partial {}^{30}Si}{\partial x} - v \cdot {}^{30}Si\right)\right) + \frac{d_s \cdot (1-\Phi)}{M_{SiO_2}} \cdot \frac{b^{30}Si}{bSi} \cdot R_D - \Phi \cdot \beta_P \frac{{}^{30}Si}{Si} - R_P \quad (9)$$

The fractionation factor β_P is introduced to express that the authigenic phase (ASi) is depleted in ^{30}Si with respect to silicic acid. It is defined as:

$$\beta_P = \frac{A^{30}Si/ASi}{{}^{30}Si/Si} \quad (10)$$

where $A^{30}Si$ is the ^{30}Si content of the authigenic phase.

The commonly used isotope ratios ($R_{30} = {}^{30}Si/{}^{28}Si$) and the mol fractions ($M_{30} = {}^{30}Si/Si$) calculated in the model are related as:

$$R_{30} = \frac{M_{30} \cdot R_{St} \cdot (R_{St}^{29} \cdot (c_R - 1) - 1)}{c_R \cdot M_{30} \cdot R_{St}^{29} + R_{St}^{30} \cdot (M_{30} - 1)} \quad (11)$$

$$M_{30} = \frac{R_{30} \cdot R_{St}^{30}}{c_R \cdot R_{St}^{29} \cdot (R_{30} - R_{St}^{30}) + R_{St}^{30} \cdot (1 + R_{30} + R_{St}^{29})} \quad (12)$$

These relations were derived from the following set of equations:

$$R_{30} = \frac{M_{30}}{M_{28}} \quad (13)$$

$$M_{28} + M_{29} + M_{30} = 1 \quad (14)$$

$$\delta^{29}Si = c_R \cdot \delta^{30}Si \quad (15)$$

with $M_{28} = {}^{28}Si/Si$ and $M_{29} = {}^{29}Si/Si$. The isotope ratios of the standard NBS28 are $R_{St}^{29} = 0.0507446$ and $R_{St}^{30} = 0.0341465$ (Ding et al., 2005) while the slope of the mass dependent kinetic fractionation amounts to $c_R = 0.51$ (Reynolds et al., 2007). The commonly used fractionation factor α_P (Hoefs, 1997):

$$\alpha_P = \frac{A^{30}Si/A^{28}Si}{{}^{30}Si/{}^{28}Si} \quad (16)$$

can be related to β_P as:

$$\alpha_P \approx \beta_P^{1.058} \quad (17)$$

The error introduced by this approximation is <0.01‰ in terms of $\Delta_P = 10^3 \ln \alpha_P$. The system of partial differential equations (mass balance equations) was solved numerically using the method-of-line-approach as implemented in MATHEMATICA version 9. Zero gradient conditions were applied at the lower boundary of the model column for both solutes and solids. The lower boundary was located at 50 cm depth well below the bioturbated zone where solids are only transported by advection. At the upper boundary, the concentrations of dissolved species (Si, ^{30}Si) were set to constant values (Si = 0.04 mM, $\delta^{30}Si = +1.4$‰) while time-dependent flux conditions were applied for the solids. The rain rate of biogenic opal and its isotopic composition were varied over time to mimic the peak in biogenic opal observed at ca. 28 cm sediment depth and the transition to heavier isotopic values of biogenic opal towards the base of the core 449-MUC19. Rain rate and isotopic composition of biogenic opal were maintained at constant values (241 μmol cm^{-2} yr^{-1}, +0.45‰) over the last 200 yr of the model period when the reactive upper section of the core (0–10 cm) was deposited.

3. RESULTS

3.1. Biogenic opal, silicic acid and cation concentrations

Biogenic opal concentrations were highly variable between the three sites and within each core profile (Fig. 1A, C, E, Table 1). Core 470-MUC29 from 145 m water depth showed the highest concentrations ranging between 10 and 27 wt%. Core 449-MUC19 from 319 m water depth had intermediate concentrations between 4 and 12 wt%, and core 549-MUC53 from 1005 m water depth had the lowest concentrations below 2 wt%.

The pore water silicic acid concentration profiles of all three cores strongly increased with increasing profile depth from lower bottom water concentrations around 40 μM (470-MUC29 and 449-MUC19) and 60 μM (549-MUC53) to pore water concentration of up to 900 μM (470-MUC29), 760 μM (449-MUC19) and 370 μM (549-MUC53) in the deeper part of the cores (Fig. 1B, D, F). Core 470-MUC29 showed the strongest increase within the upper ca. 6 cm profile depth, below which the silicic acid concentrations remained constant. Core 449-MUC19 was characterised by a strong increase from bottom water to elevated pore water concentrations within the first centimetre, then remained constant around 350 μM until ca. 6 cm profile depth, increased again and approached apparent equilibrium below ca. 30 cm profile depth. Core 549-MUC53 showed increasing concentrations in the upper ca. 8 cm profile depth, and constant concentrations below.

3.2. Stable silicon isotopes in biogenic opal and pore waters

$\delta^{30}Si_{bSi}$ could only be measured in cores 470-MUC29 and 449-MUC19, because the biogenic opal concentration in core 549-MUC53 was too low (1–2 wt%). The range in isotope compositions in both cores was similar varying between +0.6‰ and +1.2‰ in core 470-MUC29 and between +0.3‰ and +1.2‰ in core 449-MUC19 (Fig. 1A, C, Table 1) but the downcore patterns differed significantly. Core 470-MUC29 showed similar values near +1‰ in the deepest and shallowest parts of the profile and minimum and maximum values of +0.6‰ and +1.2‰ close to each other at intermediate depths. In contrast, core 449-MUC19 showed low $\delta^{30}Si_{bSi}$ near +0.5‰ in the upper ca. 25 cm core depth and a sharp increase to +1.2‰ below 25 cm.

The bottom water $\delta^{30}Si$ values for discrete Niskin bottle samples collected at 10°S and 12°S varied between +1.5‰ at 140 m water depth, +1.4‰ at 328 m water depth and +1.1‰ at 1000 m water depth (Fig. 1B, D, F) (Ehlert et al., 2012; Grasse et al., 2013). At site 449-MUC19 dissolved $\delta^{30}Si$ was measured directly in the overlying bottom water of the MUC, and the value of +1.4‰ was comparable to nearby bottom water measurements.

The dissolved pore water $\delta^{30}Si_{PW}$ of core 470-MUC29 varied between +1.1‰ and +1.4‰, and are indistinguishable from each other within the uncertainties of repeated sample measurements. These values were similar to the higher $\delta^{30}Si_{bSi}$ values in the core (+1.2‰). In contrast, the $\delta^{30}Si_{PW}$ of core 449-MUC19 were significantly higher than those of core 470-MUC29. The values increased from +1.4‰ in the overlying bottom water to up to +1.9‰ within the upper 10 cm. Some variations could be observed below, but a generally decreasing trend towards $\delta^{30}Si_{PW}$ values around +1.3‰ at the bottom of the core was found. Importantly, the $\delta^{30}Si_{PW}$ in the upper 25 cm profile depth were up to 1.5‰ heavier than the $\delta^{30}Si_{bSi}$ values, whereas in deeper regions both approached similar values. In core 549-MUC53 the $\delta^{30}Si_{PW}$ varied between +1.3‰ and +1.7‰, whereby the highest values were found within the uppermost 5 cm.

4. DISCUSSION

4.1. Silica concentrations and Si isotopes

The Si isotope compositions of biogenic opal and silicic acid in the pore waters were determined to investigate the behaviour of Si isotope fractionation during processes predominantly influencing the early diagenetic turnover of Si in marine sediments. In general, pore water silicic acid concentrations and the Si fluxes across the sediment – bottom water interface are controlled by the concentration, reactivity and solubility of biogenic opal. However, surface alteration or precipitation of authigenic silicate phases can limit these processes (Mackin and Aller, 1984; Van Bennekom et al., 1991; McManus et al., 1995; Dixit and Van Cappellen, 2003).

Biogenic opal content varies greatly between the three sites of our study and within each core (Fig. 1), but at the same time biogenic opal content and $\delta^{30}Si_{bSi}$ follow similar depth trends. The variations can be attributed to the different environmental and climatic periods covered by the different cores (Ehlert et al., 2015; see Supplement for additional information). This co-variation of biogenic opal content and $\delta^{30}Si_{bSi}$ is a common trend that has been observed in several downcore records from upwelling regions. A likely explanation for this is that high productivity and high surface water silicic acid utilisation cause $\delta^{30}Si_{bSi}$ compositions to approach seawater values as well as increased biogenic opal accumulation and preservation in the sediments (Ehlert et al., 2013, 2015; Pichevin et al., 2014). On a global scale, about 92% of the biogenic opal produced in the photic zone is dissolved before burial, whereby most of the recycling occurs directly below the sediment–water interface (Tréguer and De La Rocha, 2013, and references therein). Accordingly, the diffusive flux of silicic acid from the sediments is highly variable and greatly depends on the amount of biogenic opal supplied to the sediment surface. Off Peru, benthic chamber incubation data from two sites at 11°S in 305 m and 309 m water depth revealed silicic acid fluxes of 120–200 μmol cm^{-2} yr^{-1} (0.33–0.55 μmol cm^{-2} d^{-1}) into the overlying bottom waters (Fig. 2, Table 2). These fluxes are comparable to other areas of high diatom primary productivity (e.g. ca. 230 μmol cm^{-2} yr^{-1} off Monterey; Berelson et al., 2003), and much higher compared to regions with low diatom productivity (e.g. ca. 13 μmol cm^{-2} yr^{-1} in the equatorial Pacific; Tréguer and De La Rocha, 2013).

4.2. Authigenic alumino-silicate precipitation

All three sites off Peru show downcore pore water silicic acid concentrations that asymptotically increase to maximum concentrations ranging from 900 μM at the shallowest shelf site to 370 μM at the deepest shelf site. The pore water profile at site 449-MUC19 feature a conspicuous concentration plateau (ca. 350 μM) for silicic acid at 1–6 cm depth interrupting the continuous down-core increase (Fig. 1D). The solubility of biogenic opal at ambient pressure and temperature conditions, estimated as ca. 1000 μM (Van Cappellen and Qiu, 1997a; Dixit et al., 2001; Loucaides

et al., 2012), clearly exceeds the level of this intermediate plateau. Amorphous silica formed by abiotic precipitation has an even higher solubility (Gunnarsson and Arnórsson, 2000), whereas the formation of more crystalline and less soluble SiO_2 polymorphs (quartz, opal-CT) is kinetically inhibited in marine surface sediments (Williams et al., 1985).

Condensation of Si-OH groups and Al uptake may reduce the solubility of biogenic opal in seawater to lower values near 600 μM (Dixit et al., 2001; Rickert et al., 2002), which is, however, still significantly higher than the plateau value. It is thus likely that the concentration plateau at 1–6 cm sediment depth in core 449-MUC19 was not induced by opal maturation and Al uptake but reflects a dynamic balance at which silicic acid is released by biogenic opal dissolution and re-precipitated as a less soluble authigenic phase. The Si solubility of authigenic alumino-silicates formed by biogenic opal alteration is poorly constrained. For those accumulating in Mississippi delta sediments (Presti and Michalopoulos, 2008) a solubility of ca. 220 μM in seawater has been estimated (Loucaides et al., 2010), whereas alumino-silicates formed from kaolinite-biogenic opal mixtures may have a solubility of ca. 330 μM (Dixit et al., 2001). These Si saturation values are sufficiently low to explain the plateau value. It is thus likely that authigenic alumino-silicate phases precipitate in the surface layer at this location.

Our dissolved pore water $\delta^{30}Si_{PW}$ data support this hypothesis. Lithogenic silicate has $\delta^{30}Si$ signatures close to −0.2‰ (Georg et al., 2009; Savage et al., 2013). Biogenic opal in the cores varies between +0.3‰ and +1.2‰. Simple dissolution and release from either lithogenic silicate or from biogenic opal would be expected to lead to a $\delta^{30}Si_{PW}$ that is similar to the rocks or biogenic opal if there is no fractionation during biogenic opal dissolution (Wetzel et al., 2014). If enrichment of the lighter isotopes in the fluid occurs during dissolution of biogenic opal (Demarest et al., 2009) the $\delta^{30}Si_{PW}$ should even be lighter than the opal. The increasing silicic acid concentrations with core depth and thus increasing contribution of Si with a low $\delta^{30}Si$ to the dissolved Si in the pore waters should be reflected in a downcore decrease of $\delta^{30}Si_{PW}$. What the profiles instead show, however, is either no significant change in $\delta^{30}Si_{PW}$ compared to the overlying bottom water at all (core 470-MUC29), or an initial increase in $\delta^{30}Si_{PW}$ in the uppermost 5 cm (core 549-MUC53) to 10 cm (core 449-MUC19) (Fig. 1B, D, F; Ehlert et al., 2012; Grasse et al., 2013). This initial increase is associated with the strongest increase in dissolved pore water silicic acid concentration. The following downcore decrease in $\delta^{30}Si_{PW}$ is accompanied by essentially constant dissolved pore water silicic acid concentrations. In addition, the $\delta^{30}Si_{PW}$ are the same or even higher than the $\delta^{30}Si_{bSi}$, i.e. some of the lighter Si isotopes originating from biogenic opal dissolution must have been removed, leaving the pore waters enriched with the heavier Si isotopes.

Another possibility could be that Si isotope fractionation is controlled by different kinetic regimes in the sediment column or a combination of both. In kinetic dominated reactions, e.g. during rapid precipitation, strong Si isotope fractionation has been observed enriching the solution with the heavy Si isotope (Geilert et al., 2014, 2015; Roerdink et al., 2015; Oelze et al., 2014, 2015) similar to observations in core 449-MUC19 at shallow depth above 10 cm. In settings in which forward and backward isotopic exchange rates are equal or approaching equilibrium (DePaolo, 2011), steady-state regimes might be established, in which silica concentrations remain constant, but isotope exchange (dissolution-reprecipitation) continues until initial solution values are approached. In core 449-MUC19, $\delta^{30}Si_{PW}$ values approach bottom water values in depth below 20 cm and might show steady-state isotope fractionation. However, given the silica undersaturated conditions in all three cores with respect to biogenic opal or amorphous silica (see above) rapid silica precipitation can be excluded as a process causing the enriched $\delta^{30}Si_{PW}$ near the sediment surface of cores 449-MUC19 and 549-MU53. The most likely explanation is that the heavy $\delta^{30}Si_{PW}$ are the result of the formation of solid silica in the sediments. All Si-bearing solid phases newly formed by the precipitation of silicic acid at moderate and low temperatures are depleted in the heavy ^{30}Si isotope such that the remaining silicic acid attains heavy $\delta^{30}Si$ values (Geilert et al., 2014, 2015; Roerdink et al., 2015; Oelze et al., 2014, 2015). These solid phases include amorphous silica (Geilert et al., 2014), or chert (e.g., Roerdink et al., 2015; Tatzel et al., 2015), and clays (e.g. Georg et al., 2007; Hughes et al., 2013). The formation of amorphous silica can be excluded due to its much higher solubility under ambient temperature and pressure conditions in the sediment (Gunnarsson and Arnórsson, 2000).

Hence, our pore water $\delta^{30}Si$ data and benthic flux measurements support the concept of a dynamic balance. The in-situ silicic acid fluxes determined by the lander deployment at site 449-MUC19 (120–200 μmol cm^{-2} yr^{-1}) show that biogenic opal, which is depleted in ^{30}Si with respect to seawater, is rapidly dissolved within surface sediments. The $\delta^{30}Si$ enrichment in the pore fluids relative to the biogenic opal documents that isotopically light Si is removed from the pore waters through precipitation of authigenic alumino-silicate phases, which have been found or inferred in the region before (e.g., Froelich et al., 1988; Scholz et al., 2014a).

4.3. Model calculations

A numerical transport-reaction model was set-up to further investigate this scenario. For the simulation core 449-MUC19 was chosen because it shows the most pronounced signals in both pore water silicic acid concentrations and $\delta^{30}Si_{PW}$ and therefore is most suitable for the determination of an isotope fractionation factor for the precipitating authigenic alumino-silicate. The transport-reaction model simulates the dissolution of biogenic opal deposited at the seabed and the precipitation of authigenic silicate phases. Biogenic opal was assumed to dissolve without isotopic

fractionation (Wetzel et al., 2014) whereas the precipitating solid was assumed to be isotopically lighter than the ambient pore fluids applying a fractionation factor Δ_P defined as:

$$\Delta_P = \delta^{30}Si_A - \delta^{30}Si_D \quad (18)$$

where $\delta^{30}Si_A$ represents the isotopic composition of the authigenic solid while $\delta^{30}Si_D$ is the corresponding value for silicic acid.

Rain rates of biogenic opal and the rates of biogenic opal dissolution and silica precipitation were varied until the calculated benthic flux of silicic acid (Fig. 2, Table 2) and the down-core profiles of biogenic opal and silicic acid were consistent with observations in core 449-MUC19 (Fig. 3). The model results (Table 3) show that most of the silicic acid produced by biogenic opal dissolution is released into the overlying bottom water. However, ca. 24% of the opal-derived silica are re-precipitated presumably as authigenic alumino-silicate minerals. The modelled solubility of this authigenic alumino-silicate (250 μM, Table 3) is consistent with previous observations during incubation experiments of fresh diatom opal with sediment in a seawater matrix (Loucaides et al., 2010). The precipitation rate of 56 μmol Si cm^{-2} yr^{-1} (Table 3) is lower than the rate observed in the Amazon delta (Michalopoulos and Aller, 2004). The fractionation factor Δ_P was constrained by fitting the model to the measured dissolved $\delta^{30}Si_{PW}$ data. The best fit was achieved with $\Delta_P = -2.0‰$ (Fig. 3H). Essentially the same value (−2.05‰) was previously derived for 2:1 clays formed in the Amazon Basin (Hughes et al., 2013). Below ca. 2 cm depth the pore waters of 449-MUC19 are enriched in ^{30}Si due to this precipitation process. Only the uppermost layer, where the pore water is undersaturated with respect to the authigenic phase, is depleted in ^{30}Si due to the rapid dissolution of biogenic opal (Fig. 3H). Here, the $\delta^{30}Si_{PW}$ value dropped from +1.40‰ in the overlying bottom water to a minimum value of +0.95‰ at 2 cm sediment depth. The isotopic composition of silicic acid diffusing into the overlying bottom water (+0.75‰, Table 3) reflects the mixing effects of the release of isotopically light Si from biogenic opal (+0.45‰) and the removal of light Si into authigenic phases. Silicon isotope fractionation by adsorption onto Al-hydroxide phases was previously shown in experimental studies by Oelze et al. (2015), in which varying kinetic regimes control the Si isotope fractionation. During initial high precipitation rates, they found a rapid removal of the light ^{28}Si isotope from solution, resulting in a large kinetically controlled Si isotope fractionation (comparable to the high $\delta^{30}Si$ values in the upper ca. 10 cm of 449-MUC19; Figs. 1 and 3).

Table 3
Model results for station 449-MUC19 obtained at the end of the transient simulation.

Parameter	Value
Dissolution rate of biogenic opal	234 μmol cm^{-2} yr^{-1}
Precipitation rate of authigenic phase	56 μmol cm^{-2} yr^{-1}
Benthic flux of silicic acid	181 μmol cm^{-2} yr^{-1}
$\delta^{30}Si$ of benthic flux	+0.75‰

4.4. Alteration of terrigenous silicate minerals versus reverse weathering

The transport-reaction model suggests that the relatively heavy $\delta^{30}Si_{PW}$ isotope composition of core 449-MUC19 reflects the combined process of biogenic opal dissolution and removal of pore water silicic acid by authigenic alumino-silicate minerals. Previous studies have demonstrated that sequestration of pore water or opaline silica by authigenic silicate minerals in marine sediments can either operate through dissolution of terrigenous silicate minerals and subsequent co-precipitation with the released Al (Van Cappellen and Qiu, 1997a; Dixit et al., 2001) or through reaction with Al and Fe (oxyhydr)oxides and cations (mainly K and Mg) dissolved in the pore waters (Michalopoulos and Aller, 1995, 2004; Michalopoulos et al., 2000). The latter process results in the formation of K- and Fe-rich clay minerals and is commonly referred to as reverse weathering (Mackenzie and Garrels, 1966).

The Amazon delta is a prominent example for an environment where reverse weathering takes place. Because of the abundance of Al and Fe (oxyhydr)oxides originating from tropical weathering in the drainage basin, biogenic opal is considered the limiting reactant for clay mineral formation (Michalopoulos and Aller, 2004). Due to strong bottom currents and the associated regular re-working of the upper ca. 0.5–2 m of the sediment, clay mineral formation proceeds rapidly (<1 year) and is accompanied by substantial K uptake from pore water. Consequently, Amazon delta sediments are enriched in K relative to the terrigenous material and the concomitant pore waters display K concentrations below seawater concentration (Michalopoulos and Aller, 2004). In contrast to Amazon delta sediments, Peru margin sediments do not show a significant downcore variability of K/Al ratios (note a slight increase in 549-MUC53 though) and the pore waters are characterised by uniform K to Cl ratios similar to the seawater value (Fig. 4). We estimated the K uptake at station 449-MUC19 employing our solid phase data (Table 1) and simple mass balance equations. The following equation is valid for solid phase potassium at steady state:

$$K_i \cdot MAR_i - K_f \cdot MAR_f + R_K = 0 \quad (19)$$

where K_i is the K content of particles deposited at the sediment surface, K_f is the final K concentration at the base of the core, and R_k is the depth-integrated rate of K transfer from the pore water to the solid phase. The mass accumulation rate at the base of the core is estimated from porosity and ^{210}Pb data as $MAR_f = w_f\ d_S\ (1 - \Phi_f) = 0.014$ g cm^{-2} yr^{-1}. Considering that Al is a conservative tracer and assuming steady state, the initial mass accumulation rate at the sediment–water interface (MAR_i) is derived as:

$$MAR_i = \frac{Al_f}{Al_i} \cdot MAR_f \quad (20)$$

where Al_i is the initial concentration at the sediment water interface (22.27 mg g^{-1}, Table 1) and Al_f the concentration at the core base (39.88 mg g^{-1}, Table 1). Combining the equations above, the K uptake rate results as:

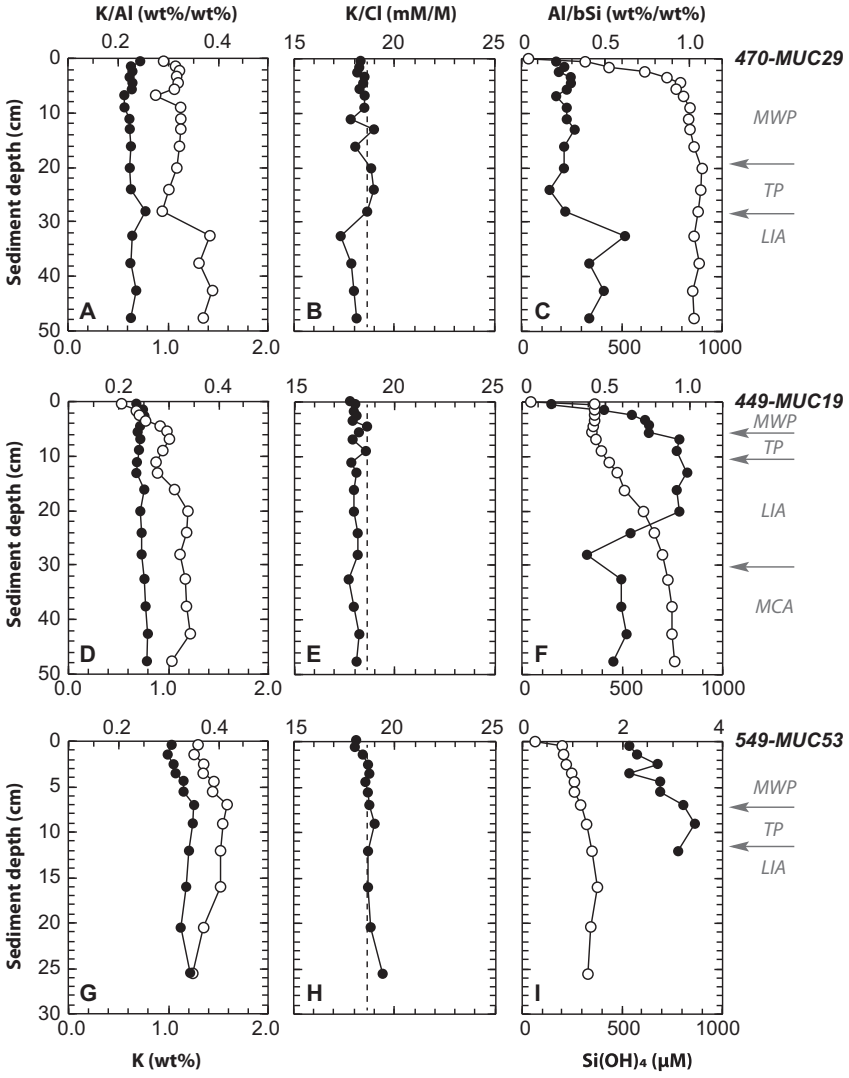

Fig. 4. Downcore profiles of (A, D, G) solid phase K/Al (solid circles) and K (open circles), (B, E, H) pore water K/Cl (the vertical dashed line depicts the K/Cl of seawater) and (C, F, I) solid phase Al/bSi ratio (solid circles) and pore water silicic acid (open circles) for all sediment cores. Note differing axis scalings for Al/bSi. Solid phase K concentrations were corrected for the K contribution from evaporated pore water. Contributions of Al from pore waters are insignificant.

$$R_K = \mathrm{MAR}_f \cdot \left(K_f - K_i \cdot \frac{Al_f}{Al_i}\right) = 0.01 \text{ mg cm}^{-2} \text{ yr}^{-1} \quad (21)$$

with $K_i = 5.26$ mg g^{-1} and $K_f = 10.27$ mg g^{-1} (Table 1). This rate can be compared to the depth-integrated rate of silica precipitation derived from the model (56 µmol cm^{-2} yr^{-1}, Table 3) that translates into a K uptake rate of 0.416 mg cm^{-2} yr^{-1} if the authigenic phase had a molar K/Si ratio of 0.19 as observed in the Amazon delta (Michalopoulos and Aller, 2004) and if all K required for the authigenic phase originated from the pore water. The rate derived from the solid phase measurements (0.01 mg cm^{-2} yr^{-1}) is much smaller than this hypothetical value (0.416 mg cm^{-2} yr^{-1}). Hence, it can be concluded that the authigenic phase at station 449-MUC19 either contains much less K than the silicates formed in Amazon delta sediments and/or that most of the K bound in this phase is not derived from the pore water but from other solid phases. Therefore, the authigenic mineral formation at our study site does not qualify as reverse weathering.

The formation of authigenic alumino-silicate minerals through dissolution of terrigenous silicate minerals and co-precipitation of the liberated Al with pore water silicic acid has been reported for opal-rich deep-sea sediments of the Southern Ocean (Van Cappellen and Qiu, 1997a). The sediment cores investigated in that study display an inverse relationship between the extent of silicic acid build-up in pore water and the ratio of the depositional flux of biogenic opal and detrital material, i.e. maximum pore water silicic acid concentrations are lower with increasing ratios of detrital material and biogenic opal. Based on this observation, the authors concluded that the simultaneous re-precipitation of Al and silicic acid prevents pore water silica

from reaching saturation with respect to the dissolving biogenic opal. This interpretation is in line with our observations. The sediment cores from the Peruvian margin studied here show a similar exponential decline in the maximum silicic acid concentrations with increasing ratios between detrital material (as represented by sedimentary Al) and biogenic opal (Fig. 5). Moreover, the plateau in the pore water silicic acid profile as well as high $\delta^{30}Si_{PW}$ up to +1.9‰ in 449-MUC19 could be explained by a higher Al availability related to a positive excursion in the Al to biogenic opal ratio in the upper 20 cm of the sediment (Fig. 4F). All three cores in this study cover a period of time (Figs. 1 and 4; see Supplement for details), during which significant climatically triggered changes in terrigenous matter supply occurred. High Al to biogenic opal ratios occur in sediment depths corresponding to the Little Ice Age, which was characterised by permanent El Nino-like conditions with higher precipitation and runoff of detrital material from land. The younger sediment layers above as well as the deeper sediments show decreasing Al to biogenic opal ratios and $\delta^{30}Si_{PW}$ values closer to the bottom water values and correspond to the Modern Warm Period and the Medieval Climate Anomaly, which are characterised by much drier conditions on land and reduced supply of terrigenous material (e.g. Sifeddine et al., 2008). In analogy to biogenic opal-rich sediments in the Southern Ocean, formation of alumino-silicate minerals in diatomaceous muds of the Peruvian continental margin is thus most likely controlled by the availability of terrigenous matter rather than biogenic opal. This assumption is consistent with the mostly dry climate on land and thus low concentrations of pure Al (oxyhydr)oxides in Peru margin sediments. Moreover, because of reductive dissolution of Fe (oxyhydr)oxides and diffusive loss of pore water Fe across the sediment-bottom water interface, sediments within the Peruvian oxygen minimum zone (470-MUC29 and 449-MUC19) are depleted rather than enriched in reactive Fe (Scholz et al., 2014a, 2014b), which may inhibit formation of Fe-rich alumino-silicates. The deeper sediments deposited below the Peruvian oxygen minimum zone (549-MUC53), however, may also represent a transition between terrigenous matter(Al)-limited and opal-limited formation of alumino-silicate minerals. Due to downslope transfer of Fe from sediments within the oxygen minimum zone, sediments below the oxygen minimum zone are enriched in reactive Fe (Scholz et al., 2014b). The higher $\delta^{30}Si_{PW}$ in shallow sediment depths of 549-MUC53 could therefore also be related to adsorption and fractionation of Si to reactive Fe (Delstanche et al., 2009). Previous studies detected or inferred high concentrations of authigenic Fe-rich silicate minerals in this area (Suits and Arthur, 2000; Scholz et al., 2014a). Consistent with this hypothesis, sediments of 549-MUC53 display a slight downcore increase in K/Al (Fig. 4G).

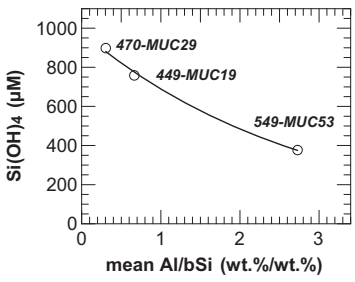

Fig. 5. Plot of the asymptotic concentrations of Si in pore waters (maximum silicic acid concentration at the lower ends of the profiles) versus mean Al/bSi for all sediment cores.

5. SUMMARY AND IMPLICATIONS

In this study we investigate the processes affecting the silicon isotope fractionation of biogenic opal and pore water silicic acid during early diagenesis in marine sediments by comparing the silicic acid and biogenic opal concentration data with their silicon isotope compositions from three short cores from the Peruvian shelf. Silicic acid fluxes reveal that a large amount of the settling biogenic opal, which is depleted in the heavy Si isotopes relative to seawater, is dissolved in the upper few millimetres directly below the sediment–water interface making these sediments an important source for isotopically light Si in marine bottom waters. At the same time, about 24% of the dissolving biogenic opal is reprecipitated as authigenic phases, most likely alumino-silicates, which form in the uppermost centimetres of the sediment profile. The Si isotope fractionation factor between authigenic precipitates and fluid is estimated to be −2.0‰, leaving the pore waters enriched in the heavy Si isotopes. The isotope composition of biogenic opal is constant within the reactive surface layer where most of the dissolution and precipitation occurs. This observation is consistent with the isotope composition of the diatoms not being significantly affected by these processes. In the Peruvian sediments, which are characterised by high biogenic opal concentrations, the precipitation process is likely controlled by terrigenous mineral supply (reactive Al). Our pioneering study suggests that Si isotopes may help to unravel the still enigmatic mechanisms responsible for the formation of authigenic silicate phases not only in the Peruvian OMZ but also in other upwelling regions.

ACKNOWLEDGEMENTS

This work is a contribution of Sonderforschungsbereich 754 "Climate – Biogeochemistry Interactions in the Tropical Ocean" (www.sfb754.de), which is supported by the Deutsche Forschungsgemeinschaft. The Seventh Framework Program of the European Union supported the participation of F.S. (Marie Curie IOF 300648, BICYCLE). We thank M. Dibbern, B. Domeyer, R. Ebbinghaus, N. Glock, J. Heinze, C. Hensen, S. Kriwanek, A. Noffke, A. Petersen, R. Surberg and M. Türk for technical assistance during sampling and analysis.

APPENDIX A. SUPPLEMENTARY DATA

Supplementary data associated with this article can be found, in the online version, at http://dx.doi.org/10.1016/j.gca.2016.07.022.

REFERENCES

Abrantes F., Lopes C., Mix A. C. and Pisias N. G. (2007) Diatoms in Southeast Pacific surface sediments reflect environmental properties. *Quatern. Sci. Rev.* **26**, 155–169. http://dx.doi.org/10.1016/j.quascirev.2006.02.022.

Albarède F., Telouk P., Blichert-Toft J., Boyet M., Agranier A. and Nelson B. K. (2004) Precise and accurate isotopic measurements using multiple-collector ICPMS. *Geochim. Cosmochim. Acta* **68**(12), 2725–2744. http://dx.doi.org/10.1016/j.gca.2003.11.024.

Berelson W. M., McManus J., Coale K. H., Johnson K. S. and Burdige D., et al. (2003) A time series of benthic flux measurements from Monterey Bay, CA. *Cont. Shelf Res.* **23**, 457–481.

Berner R. A. (1980) *Early Diagenesis – A Theoretical Approach*. Princeton University Press, Princeton.

Bohlen L., Dale A. W., Sommer S., Mosch T., Hensen C., Noffke A. and Wallmann K. (2011) Benthic nitrogen cycling traversing the Peruvian oxygen minimum zone. *Geochim. Cosmochim. Acta* **75**(20), 6094–6111. http://dx.doi.org/10.1016/j.gca.2011.08.010.

Böning P., Brumsack H.-J., Böttcher M. E., Schnetger B., Kriete C., Kallmeyer J. and Borchers S. L. (2004) Geochemistry of Peruvian near-surface sediments. *Geochim. Cosmochim. Acta* **68** (21), 4429–4451. http://dx.doi.org/10.1016/j.gca.2004.04.027.

Boudreau B. P. (1996) The diffusive tortuosity of fine-grained unlithified sediments. *Geochim. Cosmochim. Acta* **60**(16), 3139–3142.

Bruland K. W., Rue E. L., Smith G. J. and DiTullio G. R. (2005) Iron, macronutrients and diatom blooms in the Peru upwelling regime: brown and blue waters of Peru. *Mar. Chem.* **93**, 81–103. http://dx.doi.org/10.1016/j.marchem.2004.06.011.

Brzezinski M. A., Jones J. L., Beucher C. P., Demarest M. S. and Berg H. L. (2006) Automated determination of silicon isotope natural abundance by the acid decomposition of cesium hexafluosilicate. *Anal. Chem.* **78**(17), 6109–6114.

Dale A. W., Sommer S., Lomnitz U., Montes I., Treude T., Liebetrau V. and Wallmann K. (2015) Organic carbon production, mineralisation and preservation on the Peruvian margin. *Biogeosciences* **12**(5), 1537–1559. http://dx.doi.org/10.5194/bg-12-1537-2015.

De Souza G. F., Reynolds B. C., Rickli J., Frank M., Saito M. A., Gerringa L. J. A. and Bourdon B. (2012) Southern Ocean control of silicon stable isotope distribution in the deep Atlantic Ocean. *Global Biogeochem. Cycles* **26**(GB2035). http://dx.doi.org/10.1029/2011GB004141.

Delstanche S., Opfergelt S., Cardinal D., Elsass F., André L. and Delvaux B. (2009) Silicon isotopic fractionation during adsorption of aqueous monosilicic acid onto iron oxide. *Geochim. Cosmochim. Acta* **73**(4), 923–934. http://dx.doi.org/10.1016/j.gca.2008.11.014.

Demarest M. S., Brzezinski M. A. and Beucher C. P. (2009) Fractionation of silicon isotopes during biogenic silica dissolution. *Geochim. Cosmochim. Acta* **73**(19), 5572–5583. http://dx.doi.org/10.1016/j.gca.2009.06.019.

DePaolo D. J. (2011) Surface kinetic model for isotopic and trace element fractionation during precipitation of calcite from aqueous solutions. *Geochim. Cosmochim. Acta* **75**(4), 1039–1056. http://dx.doi.org/10.1016/j.gca.2010.11.020.

Ding T. P., Wan D., Bai R., Zhang Z., Shen Y. and Meng R. (2005) Silicon isotope abundance ratios and atomic weights of NBS-28 and other reference materials. *Geochim. Cosmochim. Acta* **69** (23), 5487–5494. http://dx.doi.org/10.1016/j.gca.2005.06.015.

Dixit S. and van Cappellen P. (2003) Predicting benthic fluxes of silicic acid from deep-sea sediments. *J. Geophys. Res.* **108**(C10), 3334. http://dx.doi.org/10.1029/2002JC001309.

Dixit S., Van Cappellen P. and Van Bennekom A. J. (2001) Processes controlling solubility of biogenic silica and pore water build-up of silicic acid in marine sediments. *Mar. Chem.* **73**, 333–352.

Doering K., Ehlert C., Grasse P., Crosta X., Fleury S., Frank M. and Schneider R. (2016) Differences between mono-generic and mixed diatom silicon isotope compositions trace present and past nutrient utilisation off Peru. *Geochim. Cosmochim. Acta* **177**, 30–47. http://dx.doi.org/10.1016/j.gca.2015.12.029.

Ehlert C., Grasse P., Mollier-Vogel E., Böschen T., Franz J., De Souza G. F. and Frank M. (2012) Factors controlling the silicon isotope distribution in waters and surface sediments of the Peruvian coastal upwelling. *Geochim. Cosmochim. Acta* **99**, 128–145. http://dx.doi.org/10.1016/j.gca.2012.09.038.

Ehlert C., Grasse P. and Frank M. (2013) Changes in silicate utilisation and upwelling intensity off Peru since the Last Glacial Maximum – insights from silicon and neodymium isotopes. *Quatern. Sci. Rev.* **72**, 18–35. http://dx.doi.org/10.1016/j.quascirev.2013.04.013.

Ehlert C., Grasse P., Gutiérrez D., Salvatteci R. and Frank M. (2015) Nutrient utilisation and weathering inputs in the Peruvian upwelling region since the Little Ice Age. *Climate Past* **11**, 187–202. http://dx.doi.org/10.5194/cp-11-187-2015.

Estrada M. and Blasco D. (1985) Phytoplankton assemblages in coastal upwelling areas. In *Simposio Internacional Sobre Las Areas de Afloramiento Mas Importantes del Oeste Africano (Cabo Blanco y Benguela)* (eds. C. Bas, R. Margalef and P. Rubies). Instituto de Investigaciones Pesqueras, Barcelona, pp. 379–402.

Froelich P. N., Arthur M. A., Burnett W. C., Deakin M., Hensley V., Jahnke R., Kaul L., Kim K.-H., Roe K., Soutar A. and Vathakanon C. (1988) Early diagenesis of organic matter in Peru continental margin sediments: phosphorite precipitation. *Mar. Geol.* **80**, 309–343.

Geilert S., Vroon P. Z., Roerdink D. L., Van Cappellen P. and van Bergen M. J. (2014) Silicon isotope fractionation during abiotic silica precipitation at low temperatures: Inferences from flow-through experiments. *Geochim. Cosmochim. Acta* **142**, 95–114. http://dx.doi.org/10.1016/j.gca.2014.07.003.

Geilert S., Vroon P. Z., Keller N. S., Gudbrandsson S., Stefánsson A. and van Bergen M. J. (2015) Silicon isotope fractionation during silica precipitation from hot-spring waters: evidence from the Geysir geothermal field, Iceland. *Geochim. Cosmochim. Acta* **164**, 403–427. http://dx.doi.org/10.1016/j.gca.2015.05.043.

Georg R. B., Reynolds B. C., Frank M. and Halliday A. N. (2006) New sample preparation techniques for the determination of Si isotopic compositions using MC-ICPMS. *Chem. Geol.* **235**, 95–104. http://dx.doi.org/10.1016/j.chemgeo.2006.06.006.

Georg R. B., Reynolds B. C., West A. J., Burton K. W. and Halliday A. N. (2007) Silicon isotope variations accompanying basalt weathering in Iceland. *Earth Planet. Sci. Lett.* **261**(3–4), 476–490. http://dx.doi.org/10.1016/j.epsl.2007.07.004.

Georg R. B., Zhu C., Reynolds B. C. and Halliday A. N. (2009) Stable silicon isotopes of groundwater, feldspars, and clay coatings in the Navajo Sandstone aquifer, Black Mesa, Arizona, USA. *Geochim. Cosmochim. Acta* **73**(8), 2229–2241. http://dx.doi.org/10.1016/j.gca.2009.02.005.

Govindaraju K. (1994) Compilation of working values and sample description for 383 geostandards. *Geostand. Newslett.* **18**, 1–158.

Grasse P., Ehlert C. and Frank M. (2013) The influence of water mass mixing on the dissolved Si isotope composition in the Eastern Equatorial Pacific. *Earth Planet. Sci. Lett.* **380**, 60–71. http://dx.doi.org/10.1016/j.epsl.2013.07.033.

Grasshoff K., Kremling K. and Ehrhardt M. (1999) *Methods of Seawater Analysis*. Wiley.

Gunnarsson I. and Arnórsson S. (2000) Amorphous silica solubility and the thermodynamic properties of H_4SiO_4 in the range of 0° to 350 °C at Psat. *Geochim. Cosmochim. Acta* **64**(13), 2295–2307.

Hoefs J. (1997) *Stable Isotope Geochemistry*. Springer-Verlag, Berlin.

Hughes H. J., Delvigne C., Korntheuer M., De Jong J. T. M., André L. and Cardinal D. (2011) Controlling the mass bias introduced by anionic and organic matrices in silicon isotopic measurements by MC-ICP-MS. *J. Anal. At. Spectrom.* **26**, 1892–1896.

Hughes H. J., Sondag F., Santos R. V., André L. and Cardinal D. (2013) The riverine silicon isotope composition of the Amazon Basin. *Geochim. Cosmochim. Acta* **121**, 637–651. http://dx.doi.org/10.1016/j.gca.2013.07.040.

Hurd D. C. (1972) Factors affecting solution rate of biogenic opal in seawater. *Earth Planet. Sci. Lett.* **15**(4), 411–417. http://dx.doi.org/10.1016/0012-821X(72)90040-4.

Loucaides S., Michalopoulos P., Presti M., Koning E., Behrends T. and Van Cappellen P. (2010) Seawater-mediated interactions between diatomaceous silica and terrigenous sediments: Results from long-term incubation experiments. *Chem. Geol.* **270**(1–4), 68–79. http://dx.doi.org/10.1016/j.chemgeo.2009.11.006.

Loucaides S., Koning E. and Van Cappellen P. (2012) Effect of pressure on silica solubility of diatom frustules in the oceans: Results from long-term laboratory and field incubations. *Mar. Chem.* **136–137**, 1–6. http://dx.doi.org/10.1016/j.marchem.2012.04.003.

Mackenzie F. T. and Garrels R. M. (1966) Chemical mass balance between rivers and oceans. *Am. J. Sci.* **264**(7), 507–525. http://dx.doi.org/10.2475/ajs.264.7.507.

Mackin J. E. (1987) Boron and silica behavior in salt-marsh sediments: implications for paleo-boron distributions and the early diagenesis of silica. *Am. J. Sci.* **287**, 197–241.

Mackin J. E. and Aller R. C. (1984) Dissolved Al in sediments and waters of the East China Sea: implications for authigenic mineral formation. *Geochim. Cosmochim. Acta* **48**, 281–297.

McManus J., Hammond D. E., Berelson W. M., Kilgore T. E., DeMaster D. J., Ragueneau O. G. and Collier R. W. (1995) Early diagenesis of biogenic opal: Dissolution rates, kinetics, and paleoceanographic implications. *Deep. Res. II* **42**(2–3), 871–903. http://dx.doi.org/10.1016/0967-0645(95)00035-O.

Meysman F. J. R., Boudreau B. P. and Middelburg J. J. (2005) Modeling reactive transport in sediments subject to bioturbation and compaction. *Geochim. Cosmochim. Acta* **69**, 3601–3617.

Michalopoulos P. and Aller R. C. (1995) Rapid clay mineral formation in Amazon delta sediments: reverse weathering and oceanic elemental cycles. *Science* **270**(5236), 614–617.

Michalopoulos P. and Aller R. C. (2004) Early diagenesis of biogenic silica in the Amazon delta: Alteration, authigenic clay formation, and storage. *Geochim. Cosmochim. Acta* **68**(5), 1061–1085. http://dx.doi.org/10.1016/j.gca.2003.07.018.

Michalopoulos P., Aller R. C. and Reeder R. J. (2000) Conversion of diatoms to clays during early diagenesis in tropical, continental shelf muds. *Geology* **28**, 1095–1098. http://dx.doi.org/10.1130/0091-7613.

Morley D. W., Leng M. J., Mackay A. W., Sloane H. J., Rioual P. and Battarbee R. W. (2004) Cleaning of lake sediment samples for diatom oxygen isotope analysis. *J. Paleilimnol.* **31**, 391–401.

Oelze M., von Blanckenburg F., Hoellen D., Dietzel M. and Bouchez J. (2014) Si stable isotope fractionation during adsorption and the competition between kinetic and equilibrium isotope fractionation: Implications for weathering systems. *Chem. Geol.* **380**, 161–171. http://dx.doi.org/10.1016/j.chemgeo.2014.04.027.

Oelze M., von Blanckenburg F., Bouchez J., Hoellen D. and Dietzel M. (2015) The effect of Al on Si isotope fractionation investigated by silica precipitation experiments. *Chem. Geol.* **397**, 94–105. http://dx.doi.org/10.1016/j.chemgeo.2015.01.002.

Pichevin L. E., Ganeshram R. S., Geibert W., Thunell R. C. and Hinton R. W. (2014) Silica burial enhanced by iron limitation in oceanic upwelling margins. *Nat. Geosci.* **8–13**. http://dx.doi.org/10.1038/NGEO2181.

Presti M. and Michalopoulos P. (2008) Estimating the contribution of the authigenic mineral component to the long-term reactive silica accumulation on the western shelf of the Mississippi River Delta. *Cont. Shelf Res.* **28**(6), 823–838. http://dx.doi.org/10.1016/j.csr.2007.12.015.

Rabouille C., Gaillard J. F., Tréguer P. J. and Vincendeau M. A. (1997) Biogenic silica recycling in surficial sediments across the Polar Front of the Southern Ocean (Indian Sector). *Deep. Res. II* **44**(5), 1151–1176. http://dx.doi.org/10.1016/S0967-0645(96)00108-7.

Reynolds B. C., Aggarwal J., André L., Baxter D. C., Beucher C. P., Brzezinski M. A. and Cardinal D. (2007) An inter-laboratory comparison of Si isotope reference materials. *J. Anal. At. Spectrom.* **22**(5), 561–568. http://dx.doi.org/10.1039/b616755a.

Reynolds B. C., Frank M. and Halliday A. N. (2008) Evidence for a major change in silicon cycling in the subarctic North Pacific at 2.73 Ma. *Paleoceanography* **23**(PA4219). http://dx.doi.org/10.1029/2007PA001563.

Rickert D. (2000) Dissolution kinetics of biogenic silica in marine environments. *Ber. Zur Polarforschung* **351**.

Rickert D., Schlüter M. and Wallmann K. (2002) Dissolution kinetics of biogenic silica from the water column to the sediments. *Geochim. Cosmochim. Acta* **66**(3), 439–455.

Roerdink D. L., van den Boorna S. H. J. M., Geilert S., Vroon P. Z. and van Bergen M. J. (2015) Experimental constraints on kinetic and equilibrium silicon isotope fractionation during the formation of non-biogenic chert deposits. *Chem. Geol.* http://dx.doi.org/10.1016/j.chemgeo.2015.02.038.

Savage P. S., Georg R. B., Williams H. M. and Halliday A. N. (2013) The silicon isotope composition of the upper continental crust. *Geochim. Cosmochim. Acta* **109**, 384–399. http://dx.doi.org/10.1016/j.gca.2013.02.004.

Scholz F., Severmann S., McManus J., Noffke A., Lomnitz U. and Hensen C. (2014a) On the isotope composition of reactive iron in marine sediments: Redox shuttle versus early diagenesis. *Chem. Geol.* **389**, 48–59. http://dx.doi.org/10.1016/j.chemgeo.2014.09.009.

Scholz F., Severmann S., McManus J. and Hensen C. (2014b) Beyond the Black Sea paradigm: The sedimentary fingerprint of an open-marine iron shuttle. *Geochim. Cosmochim. Acta* **127**, 368–380. http://dx.doi.org/10.1016/j.gca.2013.11.041.

Sifeddine A., Gutiérrez D., Ortlieb L., Boucher H., Velazco F., Field D. B. and Baumgartner T. (2008) Laminated sediments from the central Peruvian continental slope: A 500 year record of upwelling system productivity, terrestrial runoff and redox conditions. *Prog. Oceanogr.* **79**, 190–197. http://dx.doi.org/10.1016/j.pocean.2008.10.024.

Sommer S., Linke P., Pfannkuche O., Schleicher T., Deimling J. S. V., Reitz A. and Hensen C. (2009) Seabed methane emissions and the habitat of frenulate tubeworms on the Captain

Arutyunov mud volcano (Gulf of Cadiz). *Marine Ecol. Prog. Ser.* **382**, 69–86. http://dx.doi.org/10.3354/meps07956.

Suits N. S. and Arthur M. A. (2000) Sulfur diagenesis and partitioning in Holocene Peru shelf and upper slope sediments. *Chem. Geol.* **163**(1–4), 219–234. http://dx.doi.org/10.1016/S0009-2541(99)00114-X.

Tatzel M., von Blanckenburg F., Oelze M., Schuessler J. A. and Bohrmann G. (2015) The silicon isotope record of early silica diagenesis. *Earth Planet. Sci. Lett.* **428**, 293–303. http://dx.doi.org/10.1016/j.epsl.2015.07.018.

Tréguer P. J. and De La Rocha C. L. (2013) The world ocean silica cycle. *Ann. Rev. Marine Sci.* **5**, 477–501. http://dx.doi.org/10.1146/annurev-marine-121211-172346.

Van Bennekom A. J., Buma A. G. J. and Nolting R. F. (1991) Dissolved aluminium in the Weddell-Scotia Confluence and effect of Al on the dissolution kinetics of biogenic silica. *Mar. Chem.* **35**, 423–434. http://dx.doi.org/10.1016/S0304-4203(09)90034-2.

Van Beusekom J. E. E., Van Bennekom A. J., Tréguer P. J. and Morvan J. (1997) Aluminium and silicic acid in water and sediments of the Enderby and Crozet Basins. *Deep Res. II* **44**(5), 987–1003. http://dx.doi.org/10.1016/S0967-0645(96)00105-1.

Van Cappellen P. and Qiu L. (1997a) Biogenic silica dissolution in sediments of the Southern Ocean, I. Solubility. *Deep-Sea Res. II* **44**(5), 1109–1128.

Van Cappellen P. and Qiu L. (1997b) Biogenic silica dissolution in sediments of the Southern Ocean. II. Kinetics. *Deep Sea Res. Part II* **44**(5), 1129–1149. http://dx.doi.org/10.1016/S0967-0645(96)00112-9.

Van den Boorn S. H. J. M., Vroon P. Z. and Van Bergen M. J. (2009) Sulfur-induced offsets in MC-ICP-MS silicon-isotope measurements. *J. Anal. At. Spectrom.* **24**, 1111–1114. http://dx.doi.org/10.1039/b816804k.

Wetzel F., De Souza G. F. and Reynolds B. C. (2014) What controls silicon isotope fractionation during dissolution of diatom opal? *Geochim. Cosmochim. Acta*. http://dx.doi.org/10.1016/j.gca.2014.01.028.

Williams L. A., Parks G. A. and Crerar D. A. (1985) Silica diagenesis, I. Solubility controls. *J. Sediment. Petrol.* **55**(3), 301–311. http://dx.doi.org/10.1016/0198-0254(85)93828-2.

Wollast R. and Garrels R. M. (1971) Diffusion coefficient of silca in seawater. *Nat. Phys. Sci.* **229**, 94.

Associate editor: Silke Severmann